AIMS Mathematics, 11(10): 35795–35817.
DOI: 10.3934/math.20261387
Received: 28 July 2026
Revised: 23 September 2026
Accepted: 08 October 2026
Published: 30 October 2026

https://www.aimspress.com/journal/Math

Research article

Poisson image denoising via high-order total variation and low-rank minimization

Binbin Hao[1], **Zixuan Fang**[2], **Jing Pan**[2] **and Jianguang Zhu**[2,*]

[1] College of Science, China University of Petroleum, Qingdao 266580, China
[2] College of Mathematics and Systems Science, Shandong University of Science and Technology, Qingdao 266590, China

* **Correspondence:** Email: zhujianguang@sdust.edu.cn.

Abstract: Poisson noise is an inherent signal-dependent distortion commonly encountered in low-dose medical imaging and microscopic imaging, which poses significant challenges for image restoration models, particularly in balancing effective noise removal and fine detail preservation. In this paper, we propose a Poisson image denoising method that integrates high-order total variation (HOTV) regularization with low-rank regularization. The proposed method combines the advantages of HOTV regularization to avoid staircase artifacts and low-rank prior to retain a large amount of image details. We then employ an alternating minimization method to solve the proposed Poisson image denoising model with the combination of Chambolle's dual projection algorithm and the non-negative Garrote thresholding algorithm. Experiments on natural and medical images validate the efficacy of our method, demonstrating its superiority over multiple state-of-the-art Poisson denoising approaches in both quantitative metrics and visual perception.

Keywords: Poisson image denoising; high-order total variation; the weighted nuclear norm; alternating minimization
Mathematics Subject Classification: 49J40, 65K10, 68U10, 94A08

1. Introduction

Image denoising represents a pivotal task in the field of image processing, which has a broad application prospect. When mentioning image denoising tasks, we generally think of removing additive Gaussian noise in images. However, in image applications such as astronomical imaging [1], microscopy [2], and biomedical imaging [3,4], image degradation is caused by the unavoidable Poisson noise due to the quantum nature of light. Poisson noise fluctuates with pixel intensity, presenting significant signal-dependent and non-additive characteristics. Traditional denoising approaches [5, 6]

are originally designed for additive white Gaussian noise, which makes them incapable of handling Poisson noise effectively. Consequently, denoising images contaminated by Poisson noise has emerged as a critical research challenge in these fields.

Mathematically speaking, image generation can be described by a linear model. An image $u \in R^s$ is formed into a vector from the original image with size $N \times N$ ($s = N \times N$). The Poisson degraded image $f \in R^s$ can be formulated as

$$f = \text{Poisson}(u), \tag{1.1}$$

where Poisson$(\cdot)$ means the Poisson noise process. Since the inverse problem is usually ill-posed, most denoising procedures use some form of regularization. So far, researchers have successively proposed many methods to recover damaged images. For example, Rudin et al. [7] proposed a very successful method that removes additive Gaussian white noise by using the total variation (TV) as a regularization term. Owing to its excellent capability of noise suppression together with edge and texture preservation, the TV model has been widely adopted in image restoration tasks [8–10].

Many academics then presented a number of TV regularization-based image restoration techniques to solve Poisson noise. Le et al. [11] extended the TV model to recover Poisson images. Setzer et al. [12] focused on solving Poisson image restoration task by minimizing an energy functional that combines the Kullback–Leibler (KL) divergence as a data fidelity term with the TV regularization term. Therefore, many improved methods have been proposed to overcome this limitation. One of these methods is to use high-order TV [13] (HOTV) regularization to suppress the staircase effect to get a good recovery. Yu et al. [14] introduced a non-convex penalty into a composition of TV and HOTV, and proposed a novel non-convex hybrid model for Poisson noise removal. Jiang et al. [15] developed an alternating direction method for the HOTV based Poisson noise removal problem. Adam et al. [9] further developed a regularizer combining high-order non-convex TV and overlapping group sparsity constraints. A parallel line of research generalizes integer-order TV to fractional-order derivatives, which provide a flexible trade-off between edge preservation and smoothness. Lou et al. [16] proposed a fractional-order TV regularization for the Poisson noise deconvolution, and subsequent studies have further extended fractional-order variational models to image denoising and related tasks, showing advantages in texture preservation and noise suppression [17–19]. While fractional-order TV has shown promising results in image denoising, it typically requires additional discretization schemes and parameter tuning for the fractional order, which increases computational complexity. In contrast, HOTV regularization achieves comparable staircase suppression with a simpler integer-order formulation and well-established optimization tools. Therefore, in this paper we focus on the HOTV regularization term.

In recent years, to better deal with the structure of images, non-local similar patch-based denoising methods have been widely used in image processing. In the non-local means (NL-means) algorithm [5], a given patch is replaced by a weighted mean of similar patches. The BM3D algorithm [6] groups and stacks similar patches into a 3D array, then a denoising procedure is applied along the vertical direction. Since similar patches in an image have similar structures, if we collect all similar patches in an image and stack them as column vectors to construct a matrix, the resulting matrix exhibits the low-rank property [20]. The low-rank minimization methods [21–24] have also achieved great success in image denoising problems. However, since matrix rank minimization is non-convex and NP-hard, the nuclear norm of a matrix is defined as its sum of the singular values, and the corresponding nuclear norm minimization (NNM) is generally used as the tightest convex relaxation of low-rank

minimization. To improve the flexibility of NNM, Gu et al. [23] proposed the weighted nuclear norm minimization (WNNM) model. The WNNM model assigns larger penalties to minor singular values while imposing smaller constraints on dominant ones and hence effectively preserves image sharp edges and fine details. Zhao et al. [25] decomposed the images of similar patches into a low-rank image and a sum of Gaussian-distributed residual images, and proposed a Poisson denoising model based on non-local self-similarity (NSS). In [26], the authors proposed an NSS-based Poisson image denoising model, which combines the low rank prior and group sparse coding. Recent advances in deep learning-based approaches have led to widespread applications including in denoising [27, 28]. Nevertheless, deep learning-based denoising schemes generally demand substantial training datasets, and most deep image denoising networks are trained under the Gaussian noise assumption. In addition, massive clean reference images are required to serve as training labels during model optimization. For biomedical images and SAR images, it is difficult to obtain the ideal noise-free image. Thus, these issues undoubtedly limit their practical applications. However, existing Poisson denoising methods face a fundamental dilemma. TV-based methods run fast but rely only on local information, yielding extremely poor restoration under high noise levels. Low-rank-based methods can better preserve details, but suffer from excessively long runtime due to repeated singular value decompositions (SVDs). Motivated by this gap, this paper proposes a hybrid model and develops an efficient alternating minimization algorithm that employs non-negative Garrote thresholding, Chambolle's dual projection algorithm, and other techniques, thereby keeping the runtime within a practical range while ensuring restoration accuracy. The main contributions of this paper are summarized as follows:

• We propose a hybrid regular minimization model with HOTV and patch-based WNNM to solve the Poisson noise removal problem. By combining the advantages of HOTV regularization and the weighted nuclear norm, our model effectively mitigates the staircase artifacts associated with conventional TV-based methods, while simultaneously achieving robust noise suppression and precise edge preservation.

• We employ an alternating minimization strategy to address the Poisson denoising task. Comprehensive experimental validations reveal that the proposed method achieves outstanding performance compared with several state-of-the-art approaches, in both quantitative evaluation results and visual restoration effects.

• Simulation comparisons were made between natural images and medical images. The results show that the proposed algorithm improves the peak-signal-to-noise ratio (PSNR) and structural similarity index (SSIM).

The rest of this paper is organized as follows. Section 2 provides a concise overview of the WNNM denoising method in the low-rank minimization problem. Section 3 details our proposed model and derives an efficient alternating minimization algorithm for its solution. Section 4 gives some numerical experiments to demonstrate the performance of our method. Finally, section 5 provides several concluding remarks.

2. Preliminaries

We present some relevant background knowledge in this section.

2.1. Total variation regularization

In this work, we focus on the Poisson image denoising. Minimizing the negative log-likelihood function $-\log \mathrm{P}(f|u)$ with respect to the variable u yields the following variational minimization formulation:

$$\arg\min_{u} \langle u - f \log u, \mathbf{1} \rangle + \mu\phi(u), \tag{2.1}$$

where $\mathbf{1} \in R^s$ stands for an all-ones vector. The inner product term $\langle u - f \log u, \mathbf{1} \rangle$ corresponds to the KL divergence, a widely adopted fidelity measure for Poisson noise elimination. Here, $\phi(u)$ represents the regularization functional, while the positive constant $\mu > 0$ acts as the regularization parameter to balance fidelity and regularization. When $\phi(u) = \|\nabla u\|_1$, the regularization is the well-known TV regularization. When $\phi(u) = \|\nabla^2 u\|_1$, the regularization is the HOTV regularization. One can refer the reader to [29] for more details.

2.2. Low-rank minimization with weighted nuclear norm

Similar image patches generally exhibit a consistent underlying structure. Therefore, the matrix formed by the superposition of similar patches is a low-rank matrix. The process of group construction for low-rank matrix formation is implemented by extracting image patches, matching similar patches to exploit their consistent underlying structure, and stacking these similar patches into a unified matrix. This stacked matrix inherently exhibits a low-rank property, which serves as the foundational principle for the low-rank minimization framework with a weighted nuclear norm in image restoration and denoising tasks. It is well recognized that clean natural images generally exhibit low-rank or approximately low-rank structural characteristics in their data matrix form. Since rank minimization is an NP-hard problem, the NNM of the matrix is used as a convex relaxation of the rank minimization.

Although the NNM is widely used in rank-constrained problems, it has some limitations. In the data matrix, the larger singular values are more important; however, the nuclear norm treats all singular values equally. To address this inherent drawback, Gu et al. [23] pioneered the use of WNNM as a regularization constraint, establishing a novel optimization formulation for Gaussian noise suppression:

$$X^* = \underset{X}{\operatorname{argmin}} \frac{1}{2}\|Y - X\|_F^2 + \|X\|_{\mathbf{w},*}, \tag{2.2}$$

where $\|X\|_{\mathbf{w},*} = \sum_{j=1}^{r} w_j \sigma_j(X)$, $\mathbf{w} = [w_1, w_2, \cdots, w_r]^T$, and w_i denotes the non-negative weight assigned to the ith singular value $\sigma_i(X)$. Although the general situation of WNNM is non-convex and presents computational challenges in its solution, Gu et al. [23] demonstrated that the solution of WNNM can achieve the global optimum of the original problem using standard convex optimization methods when the weights are non-descending. Accordingly, the optimal solution can be derived in a closed-form manner via the weighted singular-value soft-thresholding operation, which is formulated as: $X^* = US_w(\Sigma)V^T$. Here, $S_w(\Sigma)$ denotes the weighted soft-thresholding operator corresponding to the weight vector w, and its diagonal elements are defined as $S_w(\Sigma)_{ii} = \mathrm{Soft}(\Sigma_{ii}, w_i) = \max(0, \Sigma_{ii} - w_i)$.

3. Proposed algorithm for Poisson image denoising

In this section, we first describe the proposed Poisson image denoising model based on low-rank prior and HOTV regularization, then present an alternating minimization algorithm for the proposed

denoising model. In this study, we integrate low-rank constraint and HOTV regularization to construct a hybrid regularization framework. On this basis, a novel Poisson denoising model is established and expressed as:

$$\min_{u}\langle u - f\log u, \mathbf{1}\rangle + \lambda_1 \sum_{i=1}^{G} \|R_i u\|_{w,*} + \lambda_2 \|u\|_{HTV}, \tag{3.1}$$

where $\|\cdot\|_{w,*}$ refers to the weighted nuclear norm. $R_i u = \{u_{i,1}, u_{i,2}, \ldots, u_{i,n}\} \in \mathbb{R}^{m\times n}$ is the matrix formed by stacking n non-local similar patches corresponding to the reference patch u_i, which exploits the self-similarity prior of image textures. Here, m is the patch size, G is the number of patch groups, and $\|\cdot\|_{HTV}$ represents the HOTV norm. Different from traditional first-order TV regularization, this advanced regularization variant effectively suppresses undesirable staircase artifacts while retaining intricate texture details and sharp edge information. To simplify the optimization solving process, we introduce two auxiliary variables v and z for variable splitting. The original unconstrained optimization problem in Eq (3.1) can be further transformed into a constrained optimization formulation:

$$\begin{aligned} &\min_{u,v,z}\langle u - f\log u, \mathbf{1}\rangle + \lambda_1 \sum_{i=1}^{G} \|R_i v\|_{w,*} + \lambda_2 \|z\|_{HTV}, \\ &s.t. \quad v = u, z = u. \end{aligned} \tag{3.2}$$

The augmented Lagrangian function of Eq (3.2) is defined as the following form:

$$\begin{aligned} \mathcal{L}(u, v, z; b_1, b_2) =& \langle u - f\log u, \mathbf{1}\rangle + \lambda_1 \sum_{i=1}^{G} \|R_i v\|_{w,*} + \frac{\alpha_1}{2}\|u - v - b_1\|_2^2 \\ &+ \lambda_2 \|z\|_{HTV} + \frac{\alpha_2}{2}\|u - z - b_2\|_2^2, \end{aligned} \tag{3.3}$$

where $\alpha_1, \alpha_2 > 0$ are penalty parameters, and b_1, b_2 are Lagrangian multipliers. The minimization of Eq (3.3) can be obtained by finding the saddle point of the augmented Lagrangian function $\mathcal{L}(u, v, z; b_1, b_2)$. We solve the problem via an alternating minimization strategy, which iteratively optimizes the following three subproblems with respect to v, z and u, while updating the multipliers b_1, b_2 as follows:

$$\begin{cases} v^{k+1} = \underset{v}{\operatorname{argmin}}\, \mathcal{L}(u^k, v, z^k; b_1^k, b_2^k), \\ z^{k+1} = \underset{z}{\operatorname{argmin}}\, \mathcal{L}(u^k, v^{k+1}, z; b_1^k, b_2^k), \\ u^{k+1} = \underset{u}{\operatorname{argmin}}\, \mathcal{L}(u, v^{k+1}, z^{k+1}; b_1^k, b_2^k), \end{cases} \tag{3.4}$$

and the updated scheme of the lagrange multipliers is

$$\begin{cases} b_1^{k+1} = b_1^k - (u^{k+1} - v^{k+1}), \\ b_2^{k+1} = b_2^k - (u^{k+1} - z^{k+1}), \end{cases} \tag{3.5}$$

where k represents the kth iteration of the algorithm. In the following part, we present a detailed derivation of the procedure for Eq (3.4). For simplicity, we omit the iteration superscripts of all symbols in the subsequent analysis. We proceed to solve the subproblems sequentially.

3.1. The v-subproblem

With z and u fixed, the subproblem for v in (3.5) is

$$v = \arg\min_{v} \frac{\alpha_1}{2}\|u - v - b_1\|_2^2 + \lambda_1 \sum_{i=1}^{G} \|R_i v\|_{w,*}. \tag{3.6}$$

We adopt an overlapping patch-extraction scheme with stride $s < \sqrt{m}$, which is essential for fully exploiting NSS and avoiding blocking artifacts. Under this overlap, the identity $\sum_i R_i^\top R_i = I$ no longer holds. Following [23, 24] we use the standard patch-decoupling approximation:

$$\frac{\alpha_1}{2}\sum_{i=1}^{G} \|u - v - b_1\|_2^2 \approx \frac{\alpha_1}{2}\sum_{i=1}^{G} \|(R_i u - R_i b_1) - R_i v\|_F^2, \tag{3.7}$$

which is exact in the non-overlapping case and introduces a controllable error otherwise. Under (3.7), the objective separates over the patch groups, and each group is obtained by approximately solving:

$$\min_{R_i v} \frac{1}{2}\|B_1 - R_i v\|_F^2 + \frac{\lambda_1}{\alpha_1}\|R_i v\|_{w,*}, \qquad B_1 = R_i u - R_i b_1. \tag{3.8}$$

Let $B_1 = U\,\mathrm{diag}(\delta_1, \ldots, \delta_r)\,V^\top$ be the SVD of B_1, where $\delta_j = \sigma_j(B_1)$ and $r = \min(m, n)$. Problem (3.8) is a WNNM problem, whose exact solution is the soft-thresholding formula of [23]. Instead of this exact solver, we adopt the non-negative Garrote thresholding as a lightweight approximate solver, which retains the dominant singular values with less shrinkage bias at the cost of a controllable bounded error. The approximate solution of (3.8) is

$$R_i v = U\,\mathrm{diag}(t_1, \ldots, t_r, 0, \ldots)\,V^\top, \qquad t_j = \mathrm{gar}_{w_j}(\delta_j) = \max\Big(0,\ \delta_j - \frac{w_j^2}{\delta_j}\Big), \tag{3.9}$$

where $S_{w_j}^{G}$ denotes the non-negative Garrote shrinkage. The variance-corrected singular values and the weights are defined by

$$\hat{\sigma}_j = \sqrt{\max(0,\ \delta_j^2 - c_2)}, \qquad w_j = \frac{c_1\sqrt{n}\sigma^2}{\hat{\sigma}_j + \varepsilon}, \qquad j = 1, \ldots, r, \tag{3.10}$$

where n is the number of similar patches in the group, $c_2 = n\sigma^2$ is a constant that controls the shrinkage of singular values, and $\varepsilon > 0$ avoids division by zero. The constant c_1 absorbs the alternating direction method of multipliers (ADMM) factor λ_1/α_1 appearing in (3.8). After solving all groups, the full image is reconstructed by weighted aggregation with per-pixel coverage normalization $v = \left(\sum_i R_i^\top R_i\right)^{-1} \sum_i R_i^\top \bar{v}_i$.

3.2. z subproblem

To streamline the derivation and enhance notational compactness, we set $B_2 = u - b_2$. Given u, the minimization problem in Eq (3.4) for the z subproblem reduces to the following formula:

$$z = \underset{z}{\mathrm{argmin}} \frac{\alpha_2}{2}\|u - z - b_2\|_2^2 + \lambda_2\|z\|_{HTV}$$

$$= \underset{z}{\operatorname{argmin}} \frac{\alpha_2}{2}\|B_2 - z\|_2^2 + \lambda_2\|z\|_{HTV}, \tag{3.11}$$

where $B_2 = u - b_2$, $\|z\|_{HTV} = \|\nabla^2 z\|_1$ denotes the second-order TV regularization. Next, we use Chambolle's projection algorithm [30] to solve the above z subproblem. The solution of Eq (3.11) can be obtained by solving the following dual projection problem:

$$\begin{aligned} &\min_p \|B_2 - \beta div^2 p\|_2^2, \\ &s.t.\ \|p_{ij}\|_2 \le 1,\ \forall 1 \le i, j \le N, \end{aligned} \tag{3.12}$$

where $\beta = \frac{\lambda_2}{\alpha_2}$ and $p = \begin{pmatrix} p^{11} & p^{12} \\ p^{21} & p^{22} \end{pmatrix}$ with $p^{st} \in R^{N\times N}$ for $s, t = 1, 2$, and $div(\cdot)$ denotes the divergence operator. The dual problem of Eq (3.12) can be efficiently solved by the following semi-implicit fixed point iteration:

$$p_{i,j}^{k+1} = \frac{p_{i,j}^k - \tau A_{i,j}^k}{1 + \tau|A_{i,j}^k|}, \tag{3.13}$$

where

$$p^0 = 0, A_{i,j}^k = (\nabla^2(div^2 p^k - \frac{B_2}{\beta}))_{i,j}, \tau \le \frac{1}{64}$$

and

$$div^2 p_{i,j}^k = D_{xx}((p^{11})_{i,j}^k) + D_{xy}^+((p^{12})_{i,j}^k) + D_{yx}^-((p^{21})_{i,j}^k) + D_{yy}((p^{22})_{i,j}^k)$$

denotes the second-order divergence of the dual field p^k; see [31] for more details. When the minimizer p^* of Eq (3.12) is determined, the solution of z can be given by the following form:

$$z = B_2 - \beta div^2 p^*. \tag{3.14}$$

As stated in the literature [31], when $\tau \le \frac{1}{64}$, $div^2 p^k$ is convergent, and as $k \to \infty$, p^k obtained using the dual method is the solution to the minimization problem (3.13).

3.3. u subproblem

With fixed v and z, the subproblem with respect to u reduces to a Poisson data-fidelity optimization formulation expressed as follows:

$$u = \underset{u}{\operatorname{argmin}} \langle u - f \log u, \mathbf{1}\rangle + \frac{\alpha_1}{2}\|u - v - b_1\|_2^2 + \frac{\alpha_2}{2}\|u - z - b_2\|_2^2. \tag{3.15}$$

The solution of Eq (3.15) can be obtained by setting the first-order derivation of u as zero, yielding the following quadratic equation:

$$(\alpha_1 + \alpha_2)u^2 - \Big(\alpha_1(v + b_1) + \alpha_2(z + b_2) - \mathbf{1}\Big)u - f = 0. \tag{3.16}$$

Therefore, the closed form solution of Eq (3.15) can be given by the following form:

$$u = \frac{b + \sqrt{b^2 + 4(\alpha_1 + \alpha_2)f}}{2(\alpha_1 + \alpha_2)}, \tag{3.17}$$

where $b = \alpha_1(v + b_1) + \alpha_2(z + b_2) - \mathbf{1}$.

The flowchart of the proposed model for Poisson image denoising is presented in Figure 1. The iterative process for solving the proposed model is summarized in Algorithm 1.

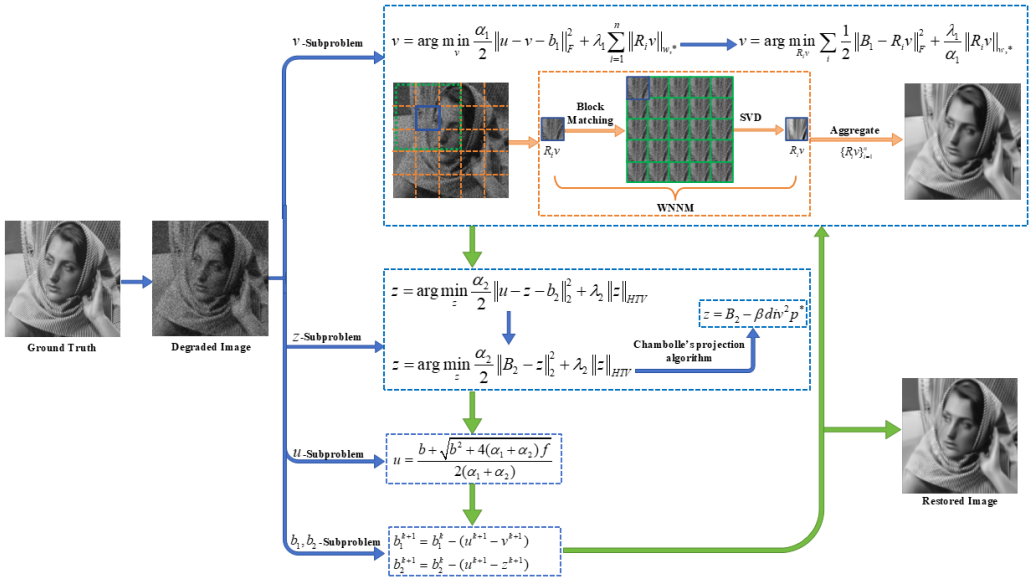


Figure 1. Flowchart of the proposed model for Poisson image denoising.

Algorithm 1: The proposed algorithm for Poisson noisy removal.

1. **Input:** The noisy image f, $b_1 = 0, b_2 = 0$, $\lambda_1, \lambda_2, \alpha_1, \alpha_2 > 0$.
2. **When the termination criterion is not satisfied**:

   (1). Update each patch group $R_i v^{k+1}$ using (3.9), and aggregate them together to get v^{k+1};

   (2). Update z^{k+1} using (3.14);

   (3). Update u^{k+1} by solving (3.17);

   (4). Update b_1^{k+1}, b_2^{k+1}:

$$b_1^{k+1} = b_1^k - (u^{k+1} - v^{k+1}),$$
$$b_2^{k+1} = b_2^k - (u^{k+1} - z^{k+1}),$$

3. **End**
4. **Output** u^{k+1}.

3.4. Convergence analysis

We analyze Algorithm 1 as a two-block ADMM. Let $w = (v, z)$, and let A be the linear operator $Au = (u, u)$, so that the constraints $u = v$, $u = z$ are equivalent to $Au = w$. Then problem (3.3) can be

rewritten as

$$\min_{u,w} \; F(u) + H(w) \quad \text{s.t.} \quad Au = w, \tag{3.18}$$

with $F(u) = \langle u - f \log u, \mathbf{1}\rangle$ and $H(w) = \lambda_1 \sum_i \|R_i v\|_{w,*} + \lambda_2 \|z\|_{HTV}$. Because H and the quadratic penalty are separable in v and z, the w-subproblem splits into the v- and z-subproblems of Algorithm 1. Thus Algorithm 1 is a two-block ADMM in which the u- and z-subproblems are solved exactly, while the v-subproblem is solved by the Garrote shrinkage (3.10), which is not the exact minimizer of (3.9) but a bounded perturbation of it.

Remark 3.1. *The patch-decoupling identity (3.9) is exact for a non-overlapping patch partition, in which $\sum_i R_i^\top R_i = I$, and is an approximation otherwise. The convergence analysis below is therefore carried out on the decoupled surrogate objective defined by (3.8); equivalently, it applies exactly in the non-overlapping case. Overlapping patch extraction with weighted aggregation is a standard numerical technique [23, 24] that improves restoration quality by fully exploiting NSS and avoiding blocking artifacts; its practical effectiveness is verified in the numerical experiments of Section 4. All convergence statements below refer to the surrogate objective actually minimized by Algorithm 1, with the Garrote inexactness absorbed into the constant $\bar{C}$.*

Lemma 3.1. *For any $y > 0$ and $w > 0$, the non-negative Garrote shrinkage $\mathrm{gar}_w(y) = \max(0,\, y - w^2/y)$ and the soft-thresholding $S_w(y) = \max(0,\, y - w)$ satisfy $|\mathrm{gar}_w(y) - S_w(y)| \le w$.*

Proof. Checking the three cases $y \ge 2w$, $w \le y < 2w$, and $0 < y < w$ yields the claim. □

Lemma 3.2. *Let $e^k = v^k_{\text{garrote}} - v^k_{\text{soft}}$ be the error at the k-th iteration induced by replacing the exact soft-thresholding solution of (3.8) with the Garrote shrinkage (3.9). Then e^k is uniformly bounded: There is a constant $\bar{C} > 0$, independent of k, such that $\|e^k\|_F \le \bar{C}$ for all k.*

Proof. By Lemma 3.1, for each group i and singular-value index j, the discrepancy is bounded by the weight $w^k_{i,j}$. From (3.10) and $\hat{\sigma}_j \ge 0$, we have $w^k_{i,j} \le c_1 \sqrt{n}\, \sigma^2/\varepsilon$. Summing over all groups and singular values, and using that the aggregation operator $\left(\sum_i R_i^\top R_i\right)^{-1} \sum_i R_i^\top$ has unit operator norm, we obtain $\|e^k\|_F \le c_1 \sqrt{n}\, \sigma^2 N_s/\varepsilon =: \bar{C}$, where $N_s = \sum_i r_i$ is the total number of singular values, a fixed finite number independent of k. □

Lemma 3.3. *The augmented Lagrangian $L(u, v, z; b_1, b_2)$ in (3.3) is bounded below on $u > 0$.*

Proof. The KL divergence $F(u) = \langle u - f \log u, \mathbf{1}\rangle$ is coercive and bounded below for $u > 0$, and all remaining terms in (3.3) are non-negative. □

Lemma 3.4. *Let $F(u) = \langle u - f \log u, \mathbf{1}\rangle$ with $f > 0$ componentwise, and let $\alpha_1, \alpha_2 > 0$. Then: (i) $u \mapsto F(u) + \frac{\alpha_1}{2}\|u - v - b_1\|_2^2 + \frac{\alpha_2}{2}\|u - z - b_2\|_2^2$ is $(\alpha_1 + \alpha_2)$-strongly convex; (ii) $v \mapsto \frac{\alpha_1}{2}\|u - v - b_1\|_F^2 + \lambda_1 \sum_i \|R_i v\|_{w,*}$ is α_1-strongly convex; (iii) $z \mapsto \frac{\alpha_2}{2}\|u - z - b_2\|_2^2 + \lambda_2 \|\nabla^2 z\|_1$ is α_2-strongly convex.*

Proof. Since $\nabla^2 F(u) = \mathrm{diag}(f_i/u_i^2) \ge 0$ on $u > 0$, F is convex. Each regularizer is convex: $\lambda_1 \sum_i \|R_i v\|_{w,*}$ is convex, since the weights w_j are non-descending (see Section 3.1), so each $R_i v\|_{w,*}$ is a unitarily invariant norm of a linear image v, and $\lambda_2 \|\nabla^2 z\|_1$ is a seminorm of a linear image of z, hence convex. The quadratic penalties have Hessians $(\alpha_1 + \alpha_2)I$, $\alpha_1 I$, and $\alpha_2 I$, respectively, hence are strongly convex with those moduli. The sum of a convex function and a μ-strongly convex function is μ-strongly convex, which proves the claim. □

Theorem 3.5. *Let $\{u^k, v^k, z^k, b_1^k, b_2^k\}$ be generated by Algorithm 1, where the v-subproblem is solved by the Garrote shrinkage (3.9) and the z-subproblem by Chambolle's iteration with step $\tau \le 1/64$. Assume $f > 0$ componentwise and $\alpha_1, \alpha_2 > 0$. Then:*

(1) The augmented Lagrangian satisfies

$$\begin{aligned}&\mathcal{L}(u^{k+1}, v^{k+1}, z^{k+1}; b_1^k, b_2^k) - \mathcal{L}(u^k, v^k, z^k; b_1^k, b_2^k)\\ &\le -\tfrac{\alpha_1}{2}\|\tilde{v}^{k+1} - v^k\|_F^2 - \tfrac{\alpha_2}{2}\|z^{k+1} - z^k\|_2^2 - \tfrac{\alpha_1+\alpha_2}{2}\|u^{k+1} - u^k\|_2^2 + \bar{C},\end{aligned} \tag{3.19}$$

where $\tilde{v}^{k+1}$ is the exact soft-thresholding minimizer of the v-subproblem and $\bar{C}$ is the uniform bound of Lemma 3.2.

(2) Summing (3.19) over $k = 0, \dots, K-1$ yields

$$\frac{1}{K}\sum_{k=0}^{K-1}\left[\tfrac{\alpha_1}{2}\|\tilde{v}^{k+1} - v^k\|_F^2 + \tfrac{\alpha_2}{2}\|z^{k+1} - z^k\|_2^2 + \tfrac{\alpha_1+\alpha_2}{2}\|u^{k+1} - u^k\|_2^2\right] \le \frac{\mathcal{L}^0 - \inf\mathcal{L}}{K} + \bar{C},$$

so the successive step sizes are $O(\bar{C})$ on average; they vanish in the Cesàro sense as $\bar{C} \to 0$.

(3) Every limit point (u^*, v^*, z^*) of the sequence (whenever such a point exists) satisfies the first-order optimality conditions of the surrogate problem up to a residual of order $O(\bar{C})$; as $\bar{C} \to 0$ the residual vanishes, and (u^*, v^*, z^*) is a Karush-Kuhn-Tucker (KKT) point of (3.2).

Proof. (1) Let $\tilde{v}^{k+1}$ be the exact (soft-thresholding) minimizer of the v-subproblem, so that $v^{k+1} = \tilde{v}^{k+1} + e^{k+1}$ with $\|e^{k+1}\|_F \le \bar{C}$. By Lemma 3.4(i), the u-subproblem is $(\alpha_1 + \alpha_2)$-strongly convex and is solved exactly, hence

$$\begin{aligned}&F(u^{k+1}) + \tfrac{\alpha_1}{2}\|u^{k+1} - v^{k+1} - b_1^k\|_F^2 + \tfrac{\alpha_2}{2}\|u^{k+1} - z^{k+1} - b_2^k\|_2^2\\ \le&F(u^k) + \tfrac{\alpha_1}{2}\|u^k - v^{k+1} - b_1^k\|_F^2 + \tfrac{\alpha_2}{2}\|u^k - z^{k+1} - b_2^k\|_2^2 - \tfrac{\alpha_1+\alpha_2}{2}\|u^{k+1} - u^k\|_2^2.\end{aligned}$$

By Lemma 3.4(iii), the z-subproblem is α_2-strongly convex and solved exactly, hence

$$\tfrac{\alpha_2}{2}\|u^k - z^{k+1} - b_2^k\|_2^2 + \lambda_2\|z^{k+1}\|_{HTV} \le \tfrac{\alpha_2}{2}\|u^k - z^k - b_2^k\|_2^2 + \lambda_2\|z^k\|_{HTV} - \tfrac{\alpha_2}{2}\|z^{k+1} - z^k\|_2^2,$$

and, by Lemma 3.4(ii), the exact v-minimizer $\tilde{v}^{k+1}$ satisfies

$$\tfrac{\alpha_1}{2}\|u^k - \tilde{v}^{k+1} - b_1^k\|_F^2 + \lambda_1\sum_i\|R_i\tilde{v}^{k+1}\|_{w,*} \le \tfrac{\alpha_1}{2}\|u^k - v^k - b_1^k\|_F^2 + \lambda_1\sum_i\|R_i v^k\|_{w,*} - \tfrac{\alpha_1}{2}\|\tilde{v}^{k+1} - v^k\|_F^2.$$

Since $v^{k+1} = \tilde{v}^{k+1} + e^{k+1}$ with $\|e^{k+1}\|_F \le \bar{C}$, and the objective is Lipschitz on bounded sets, there is a constant $\bar{C}_1$ such that

$$\tfrac{\alpha_1}{2}\|u^k - v^{k+1} - b_1^k\|_F^2 + \lambda_1\sum_i\|R_i v^{k+1}\|_{w,*} \le \tfrac{\alpha_1}{2}\|u^k - \tilde{v}^{k+1} - b_1^k\|_F^2 + \lambda_1\sum_i\|R_i\tilde{v}^{k+1}\|_{w,*} + \bar{C}_1.$$

Chaining these four inequalities yields

$$\mathcal{L}(u^{k+1}, v^{k+1}, z^{k+1}; b^k) - \mathcal{L}(u^k, v^k, z^k; b^k) \le -\tfrac{\alpha_1}{2}\|\tilde{v}^{k+1} - v^k\|_F^2 - \tfrac{\alpha_2}{2}\|z^{k+1} - z^k\|_2^2 - \tfrac{\alpha_1+\alpha_2}{2}\|u^{k+1} - u^k\|_2^2 + \bar{C}_1,$$

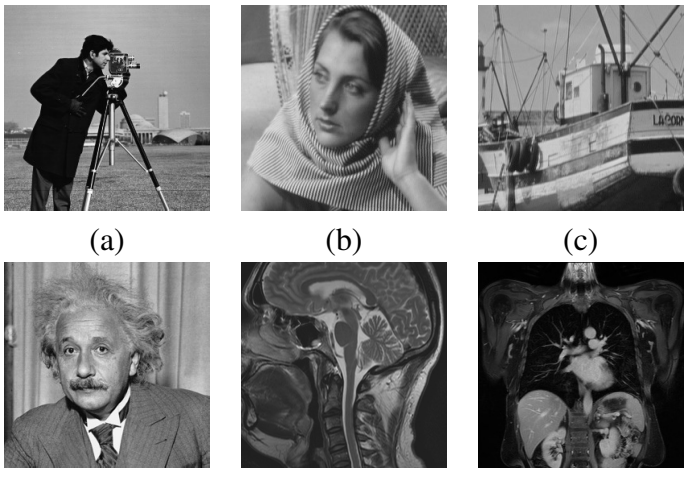
which is (3.19) with $\bar{C} = \bar{C}_1$. This proves Theorem 3.5(1).

(2) The descent inequality above, together with the uniform boundedness of the errors e^{k+1} (Lemma 3.2), is exactly the bounded-error setting of the inexact-ADMM framework [32]. By [32], the successive step sizes $\|u^{k+1} - u^k\|_2$, $\|z^{k+1} - z^k\|_2$, and $\|\tilde{v}^{k+1} - v^k\|_F$ are $O(\bar{C})$ on average, and they vanish in the Cesàro sense as $\bar{C} \to 0$. This proves Theorem 3.5(2).

(3) By the bounded-error inexact-ADMM framework [32], every limit point (u^*, v^*, z^*) of the sequence satisfies the first-order optimality conditions of the surrogate problem up to a residual of order $O(\bar{C})$; as $\bar{C} \to 0$ the residual vanishes and (u^*, v^*, z^*) is a KKT point of (3.2). This proves Theorem 3.5(3). □

4. Experimental results

In this section, we detail the effectiveness of the proposed model in terms of noise removal through extensive quantitative and qualitative experiments. We chose six typical images "Cameraman", "Barbara", "Boat", "Einstein", "Brain" and "Liver" as the test image, as shown in Figure 2. We compare our method with several state-of-the-art Poisson denoising methods, including FOTV [16], p-HONOGSTV [9], LRS [25], LRPD [20], and LRGSC [26]. Among them, FOTV and p-HONOGSTV are two recent promising TV-based Poisson denoising methods, and LRS, LRPD, and LRGSC are recent representative low-rank prior-based methods for Poisson noise removal. All compared methods are manually tuned to achieve their optimal performance or adopt their recommended parameter settings.



(a) (b) (c)

(d) (e) (f)

Figure 2. Test images: (a) Cameraman (256 × 256), (b) Barbara (256 × 256), (c) Boat (256 × 256), (d) Einstein (256 × 256), (e) Brain (442 × 442), (f) Liver (320 × 320). "Brain" and "Liver" are resized to 256 × 256 for all experiments.

Since Poisson noise is signal-dependent, its intensity is inherently determined by the pixel values of the underlying clean image. To generate Poisson noise at different levels, we scale each clean image u to peak intensity $P \in \{15, 30, 100, 155\}$ by $\tilde{u} = P \cdot u / \max(u)$, and then generate noisy observations pixel-wise as $g_i \sim \text{Poisson}(\tilde{u}_i)$ using MATLAB's `poissrnd`. This preserves the signal-dependent

property $\mathrm{Var}(f_i) = \tilde{u}_i$, with lower P indicating higher noise. We generally choose the PSNR and SSIM as indexes for quantitative analysis of image quality. PSNR is computed with the peak value P as the reference: $\mathrm{PSNR} = 10\log_{10}\left(\frac{P^2}{\mathrm{MSE}}\right)$, where MSE is the mean squared error between the original image and the processed image. Generally, a higher PSNR value and an SSIM closer to 1 indicate more accurate image recovery. In order to fairly compare the advantages of different methods, the stopping criterion for all methods is set as follows: $\frac{\|u^k - u^{k-1}\|_2}{\|u^k\|_2} \leq 10^{-3}$.

All numerical experiments conducted in this work are executed under the Windows 10 64-bit operating system with Matlab R2016a. The hardware platform is an ASUS laptop equipped with an Intel Core i5-7200 processor running at 2.50GHz and 12GB physical memory.

4.1. Parameters setting

To achieve the high-quality reconstruction performance, we investigate the influence of the parameter settings. By adjusting the parameters in turn, the set of parameters when PSNR almost reaches the highest value is the best. In the process of constructing groups, the optimal number of similar patch (patch number), the searching window (search window) and the patch size (patch size) have a great influence on the experimental results. In this subsection, we perform parameter adjustment experiments to determine the optimal values of the above parameters. Tables 1–3 show the PSNR and SSIM values obtained by the proposed method under different noise levels and with different parameter settings. Based on the single-parameter sweep results in Tables 1–3, the optimal settings are patch number = 30, search window = 20×20, and patch size = 7×7. These settings are then adopted as the final configuration for the comparative experiments in Tables 6–7.

Table 1. PSNR and SSIM values of proposed method with different patch numbers.

peak	Image	30	40	50	60
		PSNR/SSIM	PSNR/SSIM	PSNR/SSIM	PSNR/SSIM
15	Cameraman	**26.14/0.654**	24.82/0.588	24.70/0.612	24.60/0.629
	Barbara	**24.78/0.713**	24.56/0.677	24.48/0.686	24.37/0.667
30	Cameraman	26.99/0.732	**27.02/0.759**	27.01/0.743	27.00/0.734
	Barbara	**26.57/0.789**	26.44/0.786	26.34/0.778	26.30/0.765
100	Boat	**30.73/0.872**	30.42/0.867	30.39/0.867	30.29/0.866
	Einstein	**30.01/0.792**	29.99/0.787	29.93/0.785	29.96/0.786
155	Boat	31.95/0.902	**32.00/0.903**	31.92/0.901	31.83/0.900
	Einstein	**31.08/0.817**	31.01/0.816	30.95/0.813	30.84/0.814
Average		**28.53 / 0.783**	28.28 / 0.772	28.22 / 0.773	28.15 / 0.770

Table 2. PSNR and SSIM values of proposed method with different search windows.

peak	Image	20×20	30×30	40×40	50×50
		PSNR/SSIM	PSNR/SSIM	PSNR/SSIM	PSNR/SSIM
	Cameraman	**26.25/0.756**	26.23/0.746	26.24/0.749	26.17/0.748
15	Barbara	**26.24**/0.771	26.23/**0.773**	26.16/0.772	26.06/0.767
	Cameraman	**27.70/0.784**	27.68/0.764	27.59/0.764	27.58/0.768
30	Barbara	27.96/0.831	**27.97/0.833**	27.91/0.831	27.83/0.829
	Boat	**31.07/0.886**	31.06/0.885	31.04/0.884	31.02/0.883
100	Einstein	30.10/0.783	**30.12/0.784**	30.11/0.784	30.09/0.783
	Boat	32.19/0.906	**32.22/0.907**	32.21/0.907	32.20/0.906
155	Einstein	**31.20/0.829**	31.18/0.828	31.16/0.826	31.15/0.824
Average		**29.09 / 0.818**	29.08 / 0.815	29.05 / 0.814	29.01 / 0.813

Table 3. PSNR and SSIM values of our proposed method with different patch sizes.

peak	Image	3×3	7×7	11×11	15×15
		PSNR/SSIM	PSNR/SSIM	PSNR/SSIM	PSNR/SSIM
	Cameraman	23.56/0.451	25.56/0.670	**26.11/0.714**	25.97/0.711
15	Barbara	25.88/0.550	25.18/0.727	25.95/0.770	**26.21/0.781**
	Cameraman	26.07/0.624	**27.88/0.763**	27.72/0.753	27.40/0.750
30	Barbara	25.69/0.721	27.80/0.826	**27.95/0.835**	27.44/0.823
	Boat	29.27/0.824	**30.96/0.886**	30.67/0.883	30.01/0.858
100	Einstein	29.33/0.780	**30.19/0.801**	30.12/0.793	29.93/0.791
	Boat	30.77/0.865	**32.08/0.907**	31.15/0.837	28.56/0.767
155	Einstein	30.41/0.802	**31.23/0.827**	30.86/0.822	29.54/0.780
Average		27.62 / 0.702	**28.86 / 0.801**	28.81 / 0.800	28.13 / 0.783

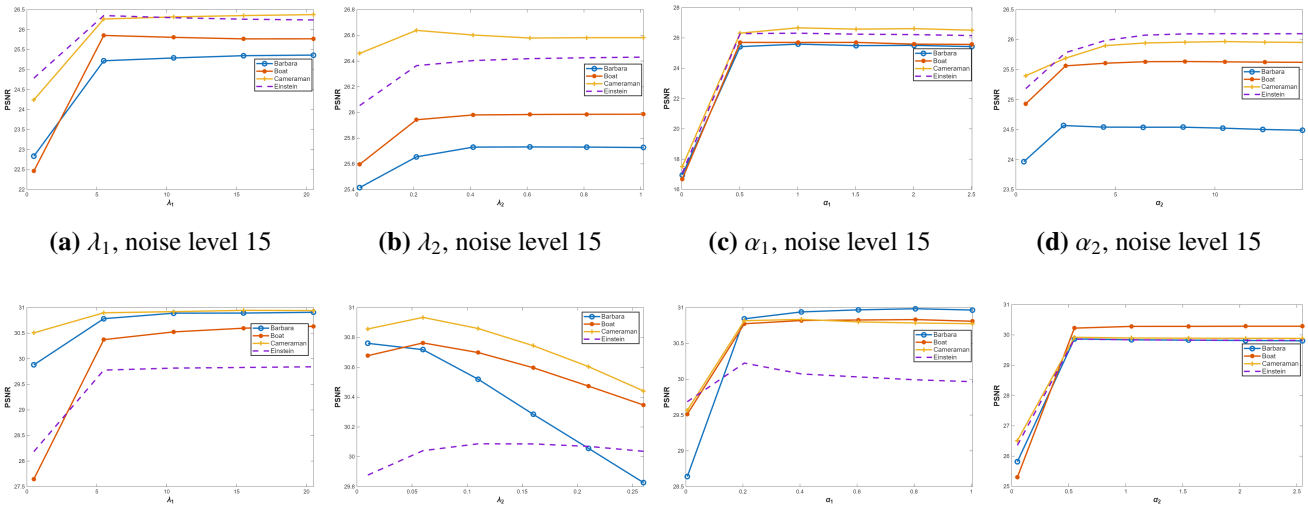
We also describe in detail the best values for the different parameters λ_1, λ_2, α_1, and α_2. To determine the optimal values of $\lambda_1, \lambda_2, \alpha_1$, and α_2, we vary each parameter in turn and record the resulting PSNR, and the value at which the PSNR reaches its maximum is selected as the optimal one. The optimal parameters obtained from the experiments are listed in Tables 4 and 5. Figure 3 shows the PSNR curves versus $\lambda_1, \lambda_2, \alpha_1$, and α_2, respectively, under the noise levels peak = 15 and peak = 100.

Table 4. Peak-dependent parameters of the proposed method.

Parameter	peak = 15	peak = 30	peak = 100	peak = 155
λ_1	10	10	15	15
λ_2	0.5	0.5	0.05	0.05
α_1	0.5	0.5	0.5	0.5
α_2	10	10	0.5	0.5

Table 5. Common parameters of the proposed method (identical for all peak values).

Parameter	Symbol	Value
Noise level	σ	–
Patch size	m	7×7
Number of similar patches	n	30
Search window	–	20×20
Patch stride	s	2
Garrote constant	c_1	$c\frac{\lambda_1}{\alpha_1}$, c is a fixed positive constant
Variance baseline	$c_2 = n\sigma^2$	–
Chambolle step	τ	0.005 $(\leq 1/64)$
Inner Chambolle iterations	–	5
Outer iterations	N_{iter}	50
Stopping tolerance	–	$\|\|u^k - u^{k-1}\|\|_2 / \|\|u^k\|\|_2 \leq 10^{-3}$



(a) λ_1, noise level 15 **(b)** λ_2, noise level 15 **(c)** α_1, noise level 15 **(d)** α_2, noise level 15

(e) λ_1, noise level 100 **(f)** λ_2, noise level 100 **(g)** α_1, noise level 100 **(h)** α_2, noise level 100

Figure 3. PSNR values versus regularization parameters λ_1 and λ_2, and penalty parameters α_1 and α_2, under different noise levels for different images.

4.2. Experiments on natural images

In these experiments, we chose four typical images: "Cameraman", "Barbara", "Boat", and "Einstein" with the size of 256×256 as the test images. The Poisson noise with peak intensities

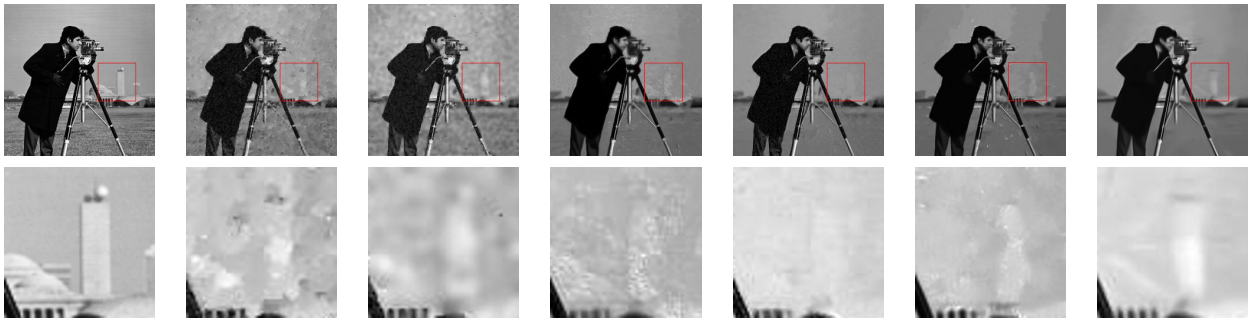
of peak = 15, 30, 100, and 155 is added to these test images to generate the noisy observations. The PSNR and SSIM results under these noise levels for all competing denoising methods are shown in Table 6. For a more comprehensive comparison, we also list the average denoising results. The best results for each case are marked in bold, and the second-best results are underlined. From Table 6, we can see that the proposed method achieves the best or comparable PSNR and SSIM in most cases, while in a few cases competing methods such as LRS and p-HONOGSTV yield slightly better results. Overall, the proposed method ranks among the top-performing methods across the tested noise levels, demonstrating competitive restoration performance. To visually demonstrate the denoising results of the proposed method, we present the visual quality of the denoised images by the different competing methods in Figures 4–7. To facilitate a detailed observation of texture preservation, a magnified view of a representative region is provided for each case.

Table 6. PSNR and SSIM values for different algorithms on natural images.

Image	Peak	FOTV	p-HONOGSTV	LRS	LRPD	LRGSC	Proposed
		PSNR/SSIM	PSNR/SSIM	PSNR/SSIM	PSNR/SSIM	PSNR/SSIM	PSNR/SSIM
Cameraman	15	24.78 / 0.639	24.65 / 0.663	25.78 / 0.724	25.64 / 0.682	26.22 / 0.741	**26.30 / 0.782**
	30	26.66 / 0.750	26.72 / 0.740	27.35 / 0.756	27.30 / 0.710	**28.00 / 0.799**	27.90 / 0.786
	100	29.36 / 0.755	29.98 / 0.844	30.22 / 0.852	30.54 / 0.833	30.89 / 0.866	**30.99 / 0.877**
	155	30.40 / 0.833	31.15 / 0.865	31.36 / 0.871	31.89 / 0.883	32.06 / 0.891	**32.21 / 0.900**
Barbara	15	22.70 / 0.596	22.68 / 0.612	25.17 / 0.734	24.79 / 0.707	25.44 / 0.735	**26.15 / 0.749**
	30	24.23 / 0.686	24.39 / 0.707	27.09 / 0.800	26.74 / 0.783	27.38 / 0.809	**28.17 / 0.841**
	100	27.52 / 0.816	27.58 / 0.838	30.34 / 0.893	30.74 / 0.905	31.11 / 0.912	**31.58 / 0.913**
	155	28.75 / 0.851	28.99 / 0.876	31.61 / 0.913	32.09 / 0.930	31.80 / 0.914	**32.78 / 0.934**
Boat	15	24.23 / 0.654	24.09 / 0.657	25.40 / 0.739	24.99 / 0.698	24.98 / 0.728	**26.01 / 0.759**
	30	25.79 / 0.716	25.98 / 0.736	27.18 / 0.789	26.63 / 0.740	27.65 / **0.807**	**27.76** / 0.806
	100	28.85 / 0.826	29.25 / 0.841	30.30 / 0.874	30.39 / 0.871	30.84 / 0.887	**31.20 / 0.889**
	155	30.02 / 0.857	30.34 / 0.866	31.40 / 0.894	31.73 / 0.904	32.05 / 0.906	**32.25 / 0.907**
Einstein	15	25.50 / 0.618	25.09 / 0.602	25.80 / 0.631	25.68 / 0.630	26.14 / 0.649	**26.46 / 0.669**
	30	26.97 / 0.678	27.00 / 0.681	27.35 / 0.691	27.03 / 0.687	27.65 / 0.707	**27.90 / 0.719**
	100	29.53 / 0.781	29.47 / 0.763	29.92 / 0.782	30.01 / 0.788	30.15 / 0.789	**30.30 / 0.797**
	155	30.49 / 0.811	30.42 / 0.797	30.87 / 0.817	**31.36 / 0.834**	31.10 / 0.824	31.31 / 0.831
Average		27.23 / 0.742	27.36 / 0.756	28.57 / 0.798	28.60 / 0.787	28.96 / 0.811	**29.28 / 0.822**

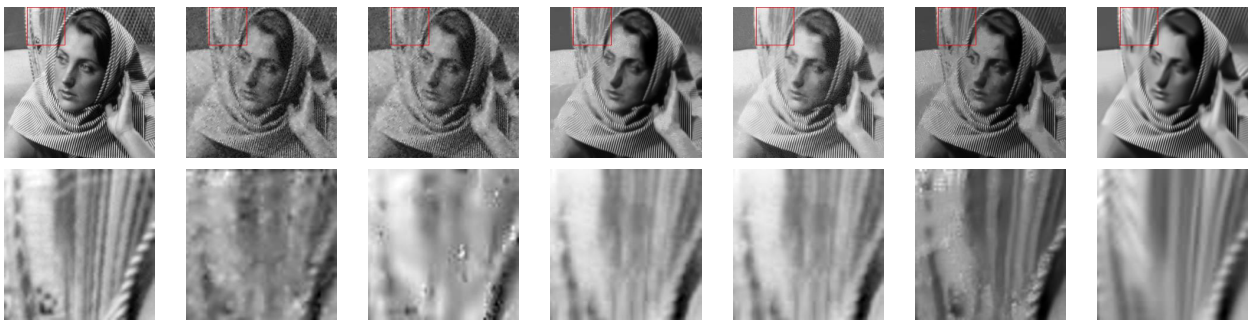
Figures 4 and 5 demonstrate the proposed method recovering more image details and preserving sharper edges from the noisy observation in high noise levels. The five compared methods can effectively remove Poisson noise, but restoring the image's quality is different. In contrast, FOTV and p-HONOGSTV can generate the pronounced ringing block effect and cannot effectively remove noise. Compared with LRS and LRPD, LRGSC recovers more texture details and edge information, while a small amount of noise still remains in the restored images. LRPD can effectively eliminate

Poisson noise yet tends to induce undesirable visual artifacts, while LRS recovers richer image details but leaves noticeable residual noise. Figures 6 and 7 present the restoration comparison results for "Boat" and "Einstein" images in low noise levels. Our proposed robust method can obtain better denoising results with a cleaner image and more details. The images restored by the LRGSC, LRPD, and LRS methods are clearer than those restored by the FOTV and p-HONOGSTV methods. However, compared to the proposed method, it is prone to losing some detailed information. It is evident that the proposed method outperforms the competing methods across all the testing noise levels, demonstrating its superior performance in Poisson image restoration.



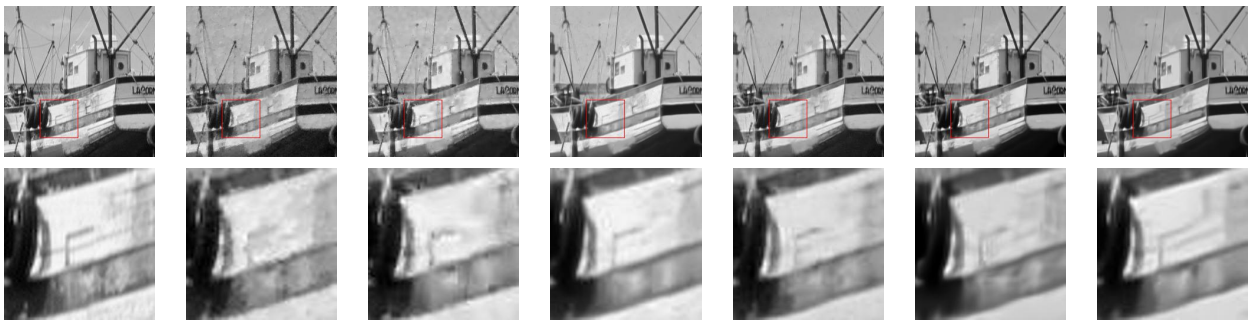
(a1) Original image (b1) FOTV (c1) p-HONOGSTV (d1) LRS (e1) LRPD (f1) LRGSC (g1) Proposed

Figure 4. The recovery results of different methods with peak = 15 on Cameraman.



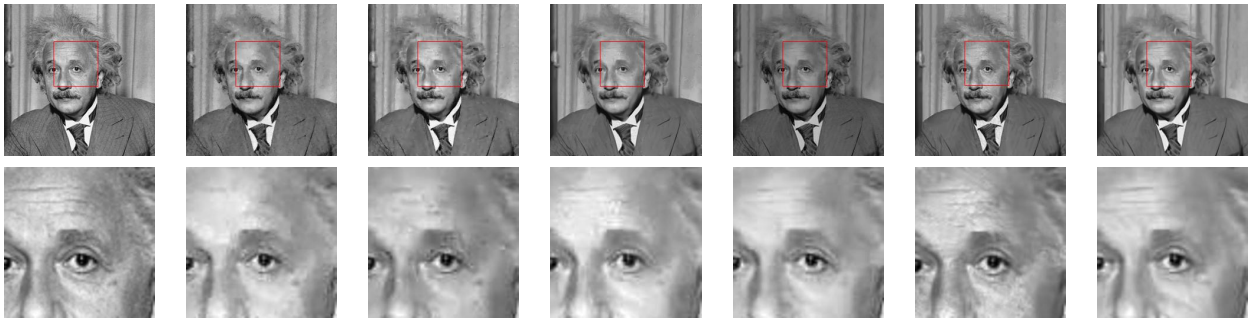
(a1) Original image (b1) FOTV (c1) p-HONOGSTV (d1) LRS (e1) LRPD (f1) LRGSC (g1) Proposed

Figure 5. The recovery results of different methods with peak = 30 on Barbara.



(a1) Original image (b1) FOTV (c1) p-HONOGSTV (d1) LRS (e1) LRPD (f1) LRGSC (g1) Proposed

Figure 6. The recovery results of different methods with peak = 100 on Boat.



(a1) Original image (b1) FOTV (c1) p-HONOGSTV (d1) LRS (e1) LRPD (f1) LRGSC (g1) Proposed

Figure 7. The recovery results of different methods with peak = 155 on Einstein.

4.3. Experiments on medical images

To verify the practical usability of the proposed algorithm outperforming other comparative methods, we select two medical images of "Brain" and "Liver" with sizes 442×442 and 320×320, respectively, as test images. To unify the data during the experiment, we scaled down the size of the medical images to 256×256 and then performed the experiments. Table 5 shows the PSNR and SSIM values of the recovered results with different methods on the test images. In the experimental tables, the optimal PSNR and SSIM results are marked in bold, and the suboptimal ones are underlined. Furthermore, average PSNR and SSIM values are computed for all competing approaches for comprehensive comparison. The quantitative results demonstrate that the proposed method achieves competitive or superior performance over alternative algorithms across most Poisson noise intensities, with a few exceptions where LRGSC or LRS performs slightly better. In order to facilitate a comprehensive visual evaluation of the performance of the proposed algorithm, we present the denoising results and the local magnification images of different methods at peak values of 15 and 30 in Figures 8 and 9, respectively. From Figures 8 and 9, we can see that FOTV and p-HONOGSTV exhibit a very poor performance at the peak values of 15 and 30. FOTV has poor denoising ability, and the recovered images are almost the same as the noise images. p-HONOGSTV has a little better denoising effect compared with the FOTV, but the recovered images appear blurred and interfere with the visual effect, and even lose a lot of image structure information. LRS preserves

more structural details than LRPD but fails to suppress noise effectively. While LRPD and LRGSC can reduce Poisson noise, they introduce unnatural artifacts that degrade visual fidelity. In contrast, the proposed method, which combines the low-rank prior and HOTV, demonstrates superior performance with preserving finer details and sharper edge structures. Our solution effectively balances the suppression of staircase effects, edge preservation, and detail restoration, making the restored images more consistent with human visual perception. Overall, the proposed algorithm possesses excellent noise suppression capability. It not only produces visually favorable reconstruction results, but also achieves competitive or superior PSNR and SSIM metrics compared with competing methods in most cases.

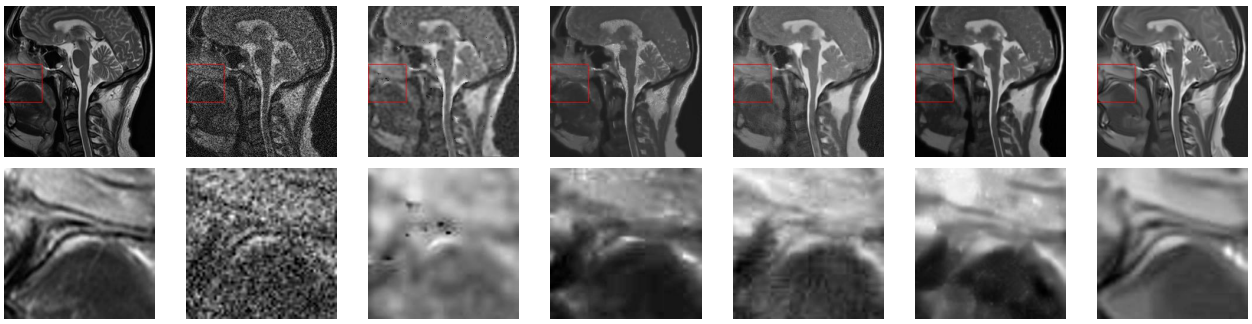


Figure 8. The recovery results of different methods with peak = 15 on Brain.

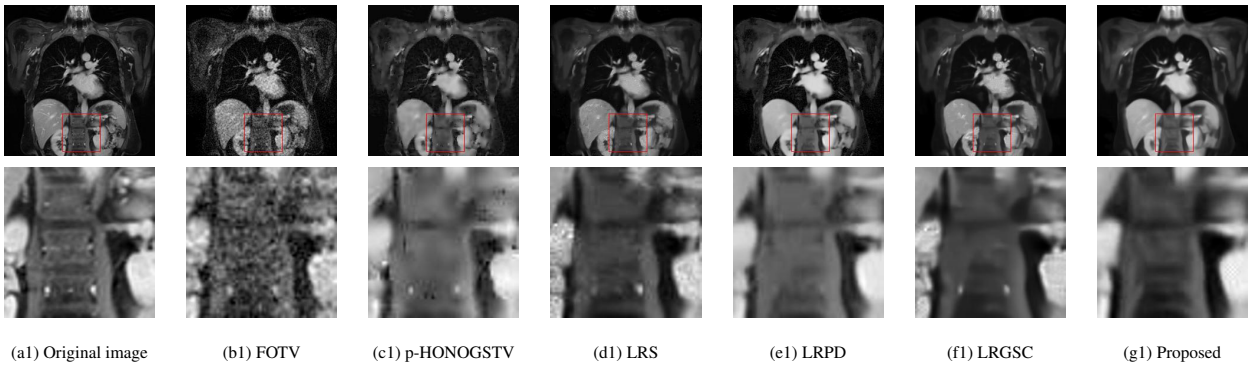


Figure 9. The recovery results of different methods with peak = 30 on Liver.

To comprehensively evaluate the computational efficiency of each algorithm, we measured the CPU runtime on medical images ("Brain" and "Liver"). The results are reported in Table 7. From the results in Table 7, it can be seen that the TV based regularization methods (FOTV and p-HONOGSTV) have the shortest runtime. However, a short runtime does not imply satisfactory restoration quality. As clearly shown in Figure 8, under high noise levels (peak = 15), the restoration results of FOTV and p-HONOGSTV are extremely poor. FOTV can hardly remove noise effectively, and the restored image is almost indistinguishable from the noisy observation; although p-HONOGSTV performs slightly better than FOTV in noise suppression, the restored images suffer from severe blurring and considerable loss of structural information, yielding unsatisfactory visual quality. In contrast, low-rank prior-based

methods (LRS, LRPD, LRGSC, and the proposed method) require longer runtime. Among the three low-rank prior-based methods, the proposed method demonstrates significant advantages in runtime. In summary, while guaranteeing denoising performance (see Table 8), the proposed method controls the runtime within a practical range of 6–8s. Compared with low-rank prior-based methods such as LRS, LRPD, and LRGSC, it exhibits significant efficiency advantages and is more suitable for practical application scenarios. More importantly, compared with "fast but ineffective" methods such as FOTV and p-HONOGSTV, the proposed method maintains excellent restoration quality even under high noise levels, truly achieving a favorable balance between computational efficiency and restoration accuracy.

Table 7. PSNR and SSIM values for different algorithms on medical images.

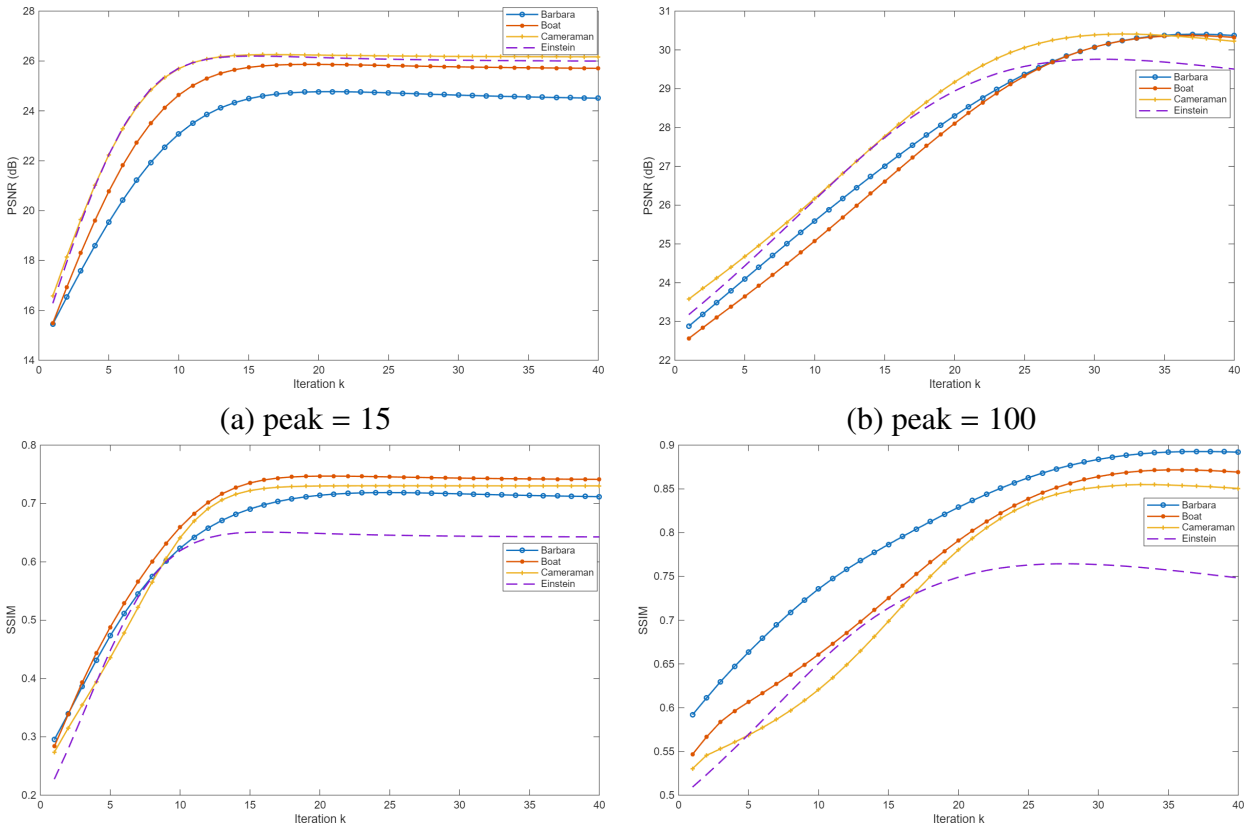
Image	Peak	FOTV	p-HONOGSTV	LRS	LRPD	LRGSC	Proposed
		PSNR/SSIM	PSNR/SSIM	PSNR/SSIM	PSNR/SSIM	PSNR/SSIM	PSNR/SSIM
Brain	15	20.16 / 0.364	26.13 / 0.716	26.98 / 0.758	26.42 / 0.715	26.75 / 0.751	**28.06 / 0.803**
	30	26.58 / 0.671	27.89 / 0.776	28.73 / 0.817	28.48 / 0.787	29.37 / 0.832	**29.81 / 0.850**
	100	30.71 / 0.847	31.03 / 0.876	32.17 / 0.898	32.09 / 0.897	32.60 / 0.907	**32.90 / 0.916**
	155	31.85 / 0.870	32.15 / 0.899	33.45 / 0.919	33.49 / 0.922	33.78 / 0.925	**34.12 / 0.933**
Liver	15	23.62 / 0.487	27.68 / 0.685	27.77 / 0.706	27.16 / 0.654	28.51 / **0.725**	**28.67** / 0.716
	30	26.74 / 0.638	29.26 / 0.768	29.60 / 0.790	29.28 / 0.751	**30.07** /0.795	29.95 / **0.806**
	100	31.99 / 0.864	32.45 / 0.889	32.93 / 0.894	32.83 / 0.891	33.10 / 0.896	**33.35** / **0.907**
	155	33.20 / 0.895	33.58 / 0.913	34.17 / 0.917	34.38 / 0.922	34.30 / 0.913	**34.58 / 0.928**
Average		28.11 / 0.705	30.02 / 0.815	30.73 / 0.837	30.52 / 0.817	31.06 / 0.843	**31.43 / 0.857**

Table 8. CPU time for different algorithms on medical images.

Image	Peak	FOTV	p-HONOGSTV	LRS	LRPD	LRGSC	Proposed
		Time(s)	Time(s)	Time(s)	Time(s)	Time(s)	Time(s)
Brain	15	0.814	1.781	16.46	70.91	63.35	7.874
	30	0.542	1.721	16.81	69.90	63.31	7.770
	100	0.809	1.717	15.03	67.91	62.67	7.274
	155	0.716	1.731	16.22	68.47	62.15	7.839
Liver	15	0.855	1.719	16.19	70.77	65.15	7.544
	30	0.655	1.706	16.61	70.99	63.15	6.839
	100	0.828	1.708	15.98	69.67	61.15	6.771
	155	0.808	1.712	16.08	69.95	60.51	6.197

4.4. Convergence verification

We also verify the good convergence of the proposed model through experiments. In Figure 10, we plot the curves of the PSNR and SSIM values versus the iteration numbers for image restoration with the noise levels peak = 15 and peak = 100, respectively. It can be visually observed from Figure 10 that as the iteration numbers increase, the PSNR and SSIM curves of the image restored by the proposed method gradually increase and become flat and stable.



(a) peak = 15 (b) peak = 100

(c) peak = 15 (d) peak = 100

Figure 10. The convergence curves of PSNR and SSIM relative to the iterations under the noise level peak = 15 and peak = 100.

5. Conclusions

In this paper, we propose a new model for recovering images disturbed by Poisson noise. The model combines two regularization terms: One is group-based low-rank regularization, and the other is pixel-based HOTV regularization. Our model performs well in suppressing the staircase effect and preserving edge details. For the proposed model, a new alternating minimization method is proposed based on Chambolle's projection algorithm and the non-negative Garrote thresholding algorithm. The experimental results show that the recovered images of the proposed method are more competitive for visual effects and image quality evaluation indexes.

Author contributions

Binbin Hao: Writing – original draft, software, methodology; Zixuan Fang: Software; Jing Pan: Software; Jianguang Zhu: Writing – review & editing, methodology, funding acquisition. All authors have read and approved the final version of the manuscript for publication.

Use of Generative-AI tools declaration

The authors declare they have not used Artificial Intelligence (AI) tools in the creation of this article.

Acknowledgments

This work was supported in part by the Qingdao Natural Science Foundation No. 25-1-1-166-zyyd-jch, and the National Natural Science Foundation of China No. U22B2049.

Data availability

Data will be made available on request.

Conflict of interest

The authors declare no conflicts of interest.

References

1. J. L. Starck, F. Murtagh, *Astronomical image and data analysis*, 2 Eds., Berlin: Springer, 2006. https://doi.org/10.1007/978-3-540-33025-7
2. J. B. Pawley, *Handbook of biological confocal microscopy*, 3 Eds., New York: Springer, 2006. http://dx.doi.org/10.1007/978-0-387-45524-2
3. M. Bertero, P. Boccacci, B. Desiderà, G. Vicidomini, Image deblurring with Poisson data: From cells to galaxies, *Inverse Probl.*, **25** (2009), 123006. http://dx.doi.org/10.1088/0266-5611/25/12/123006
4. P. Sarder, A. Nehorai, Deconvolution methods for 3-D fluorescence microscopy images, *IEEE Signal Process. Mag.*, **23** (2006), 32–45. http://dx.doi.org/10.1109/MSP.2006.1628876
5. A. Buades, B. Coll, J. Morel, A review of image denoising algorithms, with a new one, *Multiscale Model. Simul.*, **4** (2005), 490–530. http://dx.doi.org/10.1137/040616024
6. K. Dabov, A. Foi, V. Katkovnik, K. Egiazarian, Image denoising by sparse 3-D transform-domain collaborative filtering, *IEEE Trans. Image Process.*, **16** (2007), 2080–2095. http://dx.doi.org/10.1109/TIP.2007.901238
7. L. I. Rudin, S. Osher, E. Fatemi, Nonlinear total variation based noise removal algorithms, *Phys. D*, **60** (1992), 259–268. http://dx.doi.org/10.1016/0167-2789(92)90242-F

8. A. Padcharoen, D. Kitkuan, P. Kumam, J. Rilwan, W. Kumam, Accelerated alternating minimization algorithm for Poisson noisy image recovery, *Inverse Probl. Sci. Eng.*, **28** (2020), 1031–1056. http://dx.doi.org/10.1080/17415977.2019.1709454
9. T. Adam, R. Paramesran, K. Ratnavelu, A combined higher order non-convex total variation with overlapping group sparsity for Poisson noise removal, *Comp. Appl. Math.* , **41** (2022), 130. http://dx.doi.org/10.1007/s40314-022-01828-z
10. X. Zhang, An adaptive anisotropic diffusion model integrating total variation and non-local means for image denoising, *AIMS Mathematics*, **10** (2025), 28207–28220. http://dx.doi.org/10.3934/math.20251240
11. T. Le, R. Chartrand, T. J. Asaki, A variational approach to reconstructing images corrupted by Poisson noise, *J. Math. Imaging Vis.*, **27** (2007), 257–263. http://dx.doi.org/10.1007/s10851-007-0652-y
12. S. Setzer, G. Steidl, T. Teuber, Deblurring Poissonian images by split bregman techniques, *J. Vis. Commun. Image Represent.*, **21** (2010), 193–199. http://dx.doi.org/10.1016/j.jvcir.2009.10.006
13. J. Liu, T. Huang, X. Lv, S. Wang, High-order total variation-based Poissonian image deconvolution with spatially adapted regularization parameter, *Appl. Math. Modell.*, **45** (2017), 516–529. http://dx.doi.org/10.1016/j.apm.2017.01.009
14. X. Yu, Y. Peng, P. Lou, B. Huang, Poisson noise removal based on non-convex hybrid regularizers, *J. Comput. Appl. Math.*, **457** (2025), 116289. http://dx.doi.org/10.1016/j.cam.2024.116289
15. L. Jiang, J. Huang, X. G. Lv, J. Liu, Alternating direction method for the high-order total variation-based poisson noise removal problem, *Numer. Algor.*, **69** (2015), 495–516. http://dx.doi.org/10.1007/s11075-014-9908-y
16. M. R. Chowdhury, J. Zhang, J. Qin, Y. Lou, Poisson image denoising based on fractional-order total variation, *Inverse Probl. Imaging*, **14** (2020), 77–96. http://dx.doi.org/10.3934/ipi.2019064
17. A. Ben-Loghfyry, A. Hakim, A novel robust fractional-time anisotropic diffusion for multi-frame image super-resolution, *Adv. Comput. Math.*, **49** (2023), 79. http://dx.doi.org/10.1007/s10444-023-10079-3
18. A. Ben-Loghfyry, A fractional-time PDE-constrained parameter identification for inverse image noise removal problem, *J. Franklin Inst.*, **362** (2025), 107443. http://dx.doi.org/10.1016/j.jfranklin.2024.107443
19. A. Ben-Loghfyry, A. Charkaoui, A novel Perona-Malik model driven by fractional regularized diffusion mechanism with caputo derivative applied to magnetic resonance image processing, *J. Franklin Inst.*, **362** (2025), 107950. http://dx.doi.org/10.1016/j.jfranklin.2025.107950
20. P. Kumar G., R. R. Sahay, Low rank Poisson denoising (LRPD): A low rank approach using split bregman algorithm for poisson noise removal from images, In: *IEEE/CVF Conference on computer vision and pattern recognition workshops*, 2019, 1907–1916. http://dx.doi.org/10.1109/CVPRW.2019.00242
21. W. S. Dong, G. Shi, X. Li, Nonlocal image restoration with bilateral variance estimation: A low-rank approach, *IEEE Trans. Image Process.*, **22** (2013), 700–711. http://dx.doi.org/10.1109/TIP.2012.2221729

22. H. Ji, C. Liu, Z. Shen, Y. Xu, Robust video denoising using low rank matrix completion, In: *IEEE Conference on computer vision and pattern recognition*, 2010, 1791–1798. https://doi.org/10.1109/CVPR.2010.5539849

23. S. H. Gu, Q. Xie, D. Y. Meng, W. M. Zuo, X. C. Feng, L. Zhang, Weighted nuclear norm minimization and its applications to low level vision, *Int. J. Comput. Vis.*, **121** (2017), 183–208. http://dx.doi.org/10.1007/s11263-016-0930-5

24. L. Y. Ma, L. Xu, T. Y. Zeng, Low rank prior and total variation regularization for image deblurring, *J. Sci. Comput.*, **70** (2017), 1336–1357. http://dx.doi.org/10.1007/s10915-016-0282-x

25. M. C. Zhao, Y. W. Wen, M. Ng, H. W. Li, A nonlocal low rank model for poisson noise removal, *Inverse Probl. Imag.*, **15** (2021), 519–537. http://dx.doi.org/10.3934/ipi.2021003

26. J. Zhu, W. Gao, Y. Wei, B. Hao, Joint group sparse coding and weighted nuclear norm for poisson denoising, *J. Comput. Appl. Math.*, **470** (2025), 116695. http://dx.doi.org/10.1016/j.cam.2025.116695

27. H. Liang, R. Liu, Z. Wang, J. Ma, X. Tian, Variational bayesian deep network for blind poisson denoising, *Pattern Recogn.*, **143** (2023), 109810 http://dx.doi.org/10.1016/j.patcog.2023.109810

28. S. Liu, T. Zhang, R. Deng, X. Liu, H. Liu, Physics-guided deep learning framework with attention for image denoising, *Vis. Comput.*, **41** (2025), 6671–6685. http://dx.doi.org/10.1007/s00371-025-03967-w

29. C. Wu, X. Tai, Augmented lagrangian method, dual methods, and split bregman iteration for rof, vectorial tv, and high order models, *SIAM J. Imaging Sci.*, **3** (2010), 300–339. http://dx.doi.org/10.1137/090767558

30. A. Chambolle, An algorithm for total variation minimization and applications, *J. Math. Imaging Vis.*, **20** (2004), 89–97. http://dx.doi.org/10.1023/B:JMIV.0000011325.36760.1e

31. X. G. Lv, Y. Z. Song, S. X. Wang, L. Jiang, Image restoration with a high-order total variation minimization method, *Appl. Math. Modell.*, **37** (2013), 8210–8224. http://dx.doi.org/10.1016/j.apm.2013.03.028

32. M. K. Ng, F. Wang, X. Yuan, Inexact alternating direction methods for image recovery, *SIAM J. Sci. Comput.*, **33** (2011), 1643–1668. http://dx.doi.org/10.1137/100807697



AIMS Press

© 2026 the Author(s), licensee AIMS Press. This is an open access article distributed under the terms of the Creative Commons Attribution License (https://creativecommons.org/licenses/by/4.0)